

Ergodic Theory and Visualization I: Visualization of Ergodic Partition and Invariant Sets

Zoran Levnajić¹, Igor Mezić²

¹*Department of Physics and Astronomy, University of Potsdam, Karl-Liebknecht-Street 24/25, D-14476 Potsdam-Golm, Germany*

²*Department of Mechanical Engineering, University of California Santa Barbara, Santa Barbara, CA 93106, USA*

We present a computational study of the invariant sets visualization method based on ergodic partition theory, firstly proposed in [1]. The algorithms for computation of the time averages of many L^1 -functions are developed and employed producing the approximation of the ergodic partition of the phase space. The method is exposed in the context of discrete-time dynamical systems, by producing a graphical representation of the phase space in terms of the invariant set structure that gives a substantial insight into the global and local properties of the dynamics. We use the Chirikov standard map in order to show the implementation of our method, followed by applications to other higher-dimensional maps. We extend the study in our next paper [2] by studying the visualization of periodic sets using harmonic time averages constructed in [3].

Dynamical equations describing behavior of systems of scientific interest are often impossible to solve analytically, and one must resort to various computational methods approximating the actual solution. We develop a computational method for studying invariant sets of dynamical systems with arbitrary dimensionality using methods of ergodic theory. Our method consists in computing time averages of chosen functions under the phase space dynamics for a given trajectory. This allows us to obtain graphical visualization of invariant sets, including easily obtainable intersections of such sets with lower-dimensional surfaces or manifolds. The numerical efficiency of the method - interestingly - improves when the dynamics is more complex. We illustrate the utility and extent of our method by investigating the global dynamical properties of several known measure-preserving dynamical systems. In the context of dissipative systems, the method visualizes basins of attraction.

cannot be treated by purely analytical techniques, constraining one to choose among diverse computational methods. The choice of the numerical method is primarily determined by the nature of the problem, but also by the type of investigation that is to be conducted - the solution of the entire problem is often not required, and the attention is focused on the relevant results only.

On the other hand, the choice of a computational approach can be the decisive factor for the overall efficiency of investigation, as well as the precision of the results. A variety of methods had been used in the context of dynamical systems, with the direct integration of equations of motion remaining the most frequent one, both for discrete-time (maps) and continuous-time (ODEs) systems. This is the oldest numerical approach, generally straightforward to use with a vast literature behind. In this context, the visualization methods play a major role: it is often of interest to graphically visualize various aspects of motion, for instance the phase space structure of a given dynamical system.

Visualization methods generally work as algorithms for dividing the dynamics' phase space into subsets according to a prescribed property of interest. *Exit time plots* [5, 6] are computed by fixing a bounded subset of the phase space and measuring the time needed for its representative points to exit the subset, which are then colored according to their exit-times. The phase space is then sliced in the equal-exit-time regions, giving conclusions regarding the system's transport properties. The *set-oriented computational algorithms* [7, 8] allow visualization of the invariant sets and attractors

1 Introduction

The increasing range of phenomena modeled through dynamical systems [4] creates the demand for new and better computational approaches to the complex dynamics. Most of the dynamical systems problems of the current scientific interest

by appropriate subdivision of the phase space. After covering a tentative invariant region with boxes of certain (small) size, a sequence of box-size reductions is applied, and the optimal approximation of the invariant geometry is obtained at the limit. Similarly, by studying the *return time dynamics* [9] one constructs a phase space decomposition into almost invariant sets by measuring and comparing the return times for each subdivision element. A method of computing (un)stable manifolds based on analysis of *geodesic level sets* was proposed in the context of the vector fields [10], having a particular importance for control problems. In addition, a different method for approximation of the invariant manifolds was constructed by the integration of *fat trajectories* [11], as an extension of the standard numerical trajectory integration concept. A summary of (un)stable manifolds visualization methods can be found in [12].

On the other hand, ergodic theory [13] as a study of statistical aspects of motion is extensively used in the context of chaotic dynamical systems [14]. Ergodic approach to complex dynamics gave results that range from optimal mixing [15], traffic jams [16] and quantum many-body problems [17], to mathematical study of discrete dynamics [18]. Finally, employment of ergodic theory recently gave rise to new visualization methods of invariant sets, both theoretically [1, 3] and experimentally [19].

This paper presents a detailed computational study of the visualization method proposed by Mezić and Wiggins in [1]. The method consists in computation of time averages of many linearly independent L^1 -functions under a given dynamics for a grid of initial points and comparison of their values, which leads to the *ergodic partitioning* of the phase space. Given the properties of the ergodic dynamics, this partitioning results to be equivalent to decomposition of the phase space into invariant sets, whose graphical visualization will be our final aim. The method will be exposed using the well-known Chirikov standard map [20], as an example of 2D chaotic map with a rich dynamics. The method can be employed for discrete-time or continuous-time systems of arbitrary dimensionality using the appropriate slicing of the phase space by a two-dimensional surface, as well as for dissipative systems through visualizing the basins of attraction.

In contrast to the return time [9] and exit time [6] studies, our method yields the invariant set structure precisely (at the limit). It is also less numerically demanding than similar methods, as it relies on the inherent ergodicity of the dynamics. Also, the precise computation of trajectories is avoided, given that every trajectory in an ergodic set is fully included in that set.

The paper is organized as follows: after briefly discussing our method's theoretical background in Section 2., we show the time average plots for the single functions under the standard map in Section 3. The convergence of time averages is addressed in Section 4. In Section 5. we present the scatter plot analysis of the dynamics using multiple time averages and construct a simple algorithm for ergodic partition approximation. Sections 6. and 7. deal with higher-

dimensional maps like 4D Froeschlé map [21] and 3D extended standard map [22]. Conclusions are given in Section 8. In our paper to follow [2] we study further computational applications of ergodic partition theory related to the visualization of periodic sets, following the theoretical framework of Mezić and Banaszuk [3].

2 The Visualization Method

In this Section we briefly sketch the mathematical basis of our visualization method and describe its implementation algorithm. As our approach here is rather application-oriented, we will skip the rigorous proofs and refer the reader to [1] (and references therein) for more details.

2.1 The ergodic theory background

Let a discrete-time measure-preserving map $\mathbf{x}' = \mathbf{T}\mathbf{x}$ on a compact phase space A be denoted as:

$$\mathbf{x}_{n+1} = \mathbf{T}\mathbf{x}_n \quad \text{or} \quad \mathbf{x}_n = \mathbf{T}^n\mathbf{x}_0 \quad n \geq 0. \quad (1)$$

Our central aim is to visualize the *invariant sets* $B \subset A$ for the map \mathbf{T} defined as [4]:

$$\mathbf{x}_0 \in B \Rightarrow \mathbf{T}^n\mathbf{x}_0 \in B \quad \forall n \in \mathbb{Z}, \quad (2)$$

which essentially means that each trajectory that starts in an invariant set B stays in B forever.

Consider L^1 real-valued functions on A ($f : A \rightarrow \mathbb{R} \in L^1(A)$ iff $\int_A |f(\mathbf{x})| d\mathbf{x} < \infty$), and let the *time average* $f^*(\mathbf{x}_0)$ of a function $f \in L^1(A)$ corresponding to a phase space point $\mathbf{x}_0 \in A$ be defined as:

$$f^*(\mathbf{x}_0) = \lim_{n \rightarrow \infty} \frac{1}{n} \sum_{k=0}^{n-1} f(\mathbf{T}^k\mathbf{x}_0). \quad (3)$$

By the Ergodic Theorem ([13]) this limit exists almost everywhere (a.e.) in A for every $f \in L^1(A)$. We call the map \mathbf{T} *ergodic* over some set $B \subset A$ if for a.e. point $\mathbf{x}_0 \in B$ we have that the time average for every function $f \in L^1(B)$ is equal to the space average of that function f over the set B . More precisely, ergodicity over a set B means there exists an *ergodic measure* μ_B such that the ergodic equality:

$$f^*(\mathbf{x}_0) = \frac{1}{\mu_B(B)} \int_B f d\mu_B, \quad (4)$$

holds a.e. in $B \subset A$. This also implies that f^* is *constant* a.e. in $B \subset A$. Moreover, this property makes the whole set B to be accessible for a.e. trajectory; the amount of time a trajectory spends in a given region of B is proportional to the ergodic measure of that region. Also, each f^* is an *invariant function* $f^*(\mathbf{x}_0) = f^*(\mathbf{T}^n\mathbf{x}_0) \forall n$.

Let us now consider a map \mathbf{T} on a compact metric phase space A endowed with a measure μ that \mathbf{T} preserves. The set of real numbers \mathbb{R} induces a partition of A called $\zeta_f \equiv \{B_a\}_{a \in \mathbb{R}}$ through a function $f \in L^1(A)$:

$$\forall a \in \mathbb{R} \quad \exists B_a \subset A \quad \text{such that} \quad (f^*)^{-1}(a) = B_a.$$

We have: $B_a \subset A \forall a \in \mathbb{R}$, $\mu(\bigcup_a B_a) = \mu(A)$, $B_a \cap B_{a'} = \emptyset \forall a \neq a'$.

While this implies each B_a to be invariant by construction, we may still have some set B_a to actually be a union of more independent invariant sets that accidentally have the same time average for a given f . For this purpose we refine the partitioning by considering products of partitions corresponding to different functions in order to obtain a partition in which each element is a non-decomposable, ergodic and invariant set. This final *ergodic partition* ζ_e is defined as the product of all ζ_f belonging to a set $\mathcal{S} \subset L^1(A)$:

$$\zeta_e = \bigvee_{f \in \mathcal{S}} \zeta_f, \quad (5)$$

where it suffices to take \mathcal{S} to be a basis for $L^1(A)$ [1, 3].

The ergodic partition has the desired properties of dividing the phase space into a family of non-decomposable invariant sets: ergodic subsets are the "minimal observable" invariant sets. In order to visualize the ergodic sets we need to approximate the ergodic partition by computing the time averages of as many functions as possible, and observe the subsets where they are simultaneously constant. In the rest of this work we will be developing and employing a computational algorithm that uses the described idea.

2.2 The computing algorithm and numerical details

We construct the algorithm for approximation of the ergodic partition, limiting the discussion to the case of a 2D map with the phase space $A = [0, 1] \times [0, 1] \subset \mathbb{R}^2$.

step 1 Set up a grid (lattice) of initial grid-points (x_0, y_0) on the phase space A

step 2 Pick N functions $\{f_1, \dots, f_N\}$ from $L^1(A)$ and compute their partial time averages for n_{final} iterations for each grid-point, which serve as the approximations for the real time averages $\{f_1^*, \dots, f_N^*\}$

step 3 To every initial grid-point (x_0, y_0) associate its corresponding *time average vector*:

$$(x_0, y_0) \longrightarrow \tilde{\mathbf{f}}(x_0, y_0), \quad \tilde{\mathbf{f}}(x_0, y_0) = \{f_1^*(x_0, y_0), \dots, f_N^*(x_0, y_0)\} \in \mathbb{R}^N \quad (6)$$

step 4 Observe the distribution of time average vectors $\tilde{\mathbf{f}}(x_0, y_0)$ in \mathbb{R}^N and group them optimally into clusters. Divide A into a union of subsets, with each subset being given by those grid-points (x_0, y_0) whose time average vectors $\tilde{\mathbf{f}}(x_0, y_0)$ belong to the same cluster. This family of subsets is an approximation of the ergodic partition of A using N functions in the sense of Eq. (5).

The optimal number of iterations n_{final} is to be set in accordance with the convergence properties of the time averages; observe also that the quality/properties of visualization strongly depend on the way time average vector are clustered: these topic will be dealt with later.

The choice of functions $\{f_1, \dots, f_N\}$ is important: linearly dependent functions will not give a new information as their time averages differ by only a multiplicative constant. It is therefore necessary to consider linearly independent functions, which we shall do by picking them from an orthogonal basis on $L^1(A)$. We will employ the Fourier orthogonal basis and the Wavelet basis - these are actually bases for $L^2(A)$ rather than $L^1(A)$, but as we are dealing with compact metric spaces $L^2(A)$ is dense in $L^1(A)$.

The algorithm is implemented using parallel processing. Given p available processors, the phase space $A = [0, 1] \times [0, 1]$ is divided into p strips: first strip contains the grid-points from the interval $[0, \frac{1}{p}] \times [0, 1]$, and so on. After each processor computes the time averages for the grid-points in its strip, the output is given as a single grid of values. The saving factor of computing time is roughly given by the number of processors employed. All the time averages are computed simultaneously by evaluating each function at each iteration for each grid-point by its processor.

We typically use the grid of 800×800 initial grid-points and iterated the dynamics for $n_{\text{final}} = 30,000$ iterations to approximate the time average values for each function. Parallelising the computational codes is straightforward as the processors do not communicate during the run. It usually takes about 10-15 minutes to compute one function time average on a single processor for a grid of this size; a typical run was however done using 5-10 processors (depending on the availability) and took about 5 minutes for each function. Also, we sometimes computed more functions simultaneously, increasing the run time to about 7-8 minutes.

2.3 The standard map as the testing prototype

We chose the Chirikov standard map [20] for testing the performance of our method. Its behavior has been widely studied and well-understood [24, 28]. We consider it in the form:

$$\begin{aligned} x' &= x + y + \varepsilon \sin(2\pi x) \quad [\text{mod } 1] \\ y' &= y + \varepsilon \sin(2\pi x) \quad [\text{mod } 1] \end{aligned} \quad (7)$$

where $(x, y) \in [0, 1] \times [0, 1] \equiv [0, 1]^2$ (the usual standard map's parameter k is here $k = 2\pi\varepsilon$). It is an area-preserving (symplectic) map which exhibits a variety of invariant sets in form of quasi-periodic orbits, and chaotic zones that evolve in size and structure as the parameter ε is varied.

3 Single-function plots

We set $N = 1$ and consider the time averages of a single function under the dynamics of Eq.(7) for a grid of initial conditions. As the range of final time average values varies,

we adjust the coloring scheme for each plot by assigning blue to the minimum and red to the maximum value obtained.

3.1 The Fourier orthogonal basis

We pick the functions from the following functional family:

$$\sin(\pi nx + \pi my) \quad \text{with } n, m \in \mathbb{Z}, \quad (8)$$

(linearly independent for $n \neq m$), obtaining a grid of time averages corresponding to the grid of initial conditions. The time average grid is then colored, visualizing the invariant sets as the uniformly colored level sets. In Fig.1 we show three examples of time average plots for various ε -values (left), along with their phase space portraits (right). The pictures on the top deal with $\varepsilon = 0$ case, where the map possesses a family of invariant circles with $y = \text{const.}$ (a full measure of these circles have ergodic dynamics - irrational

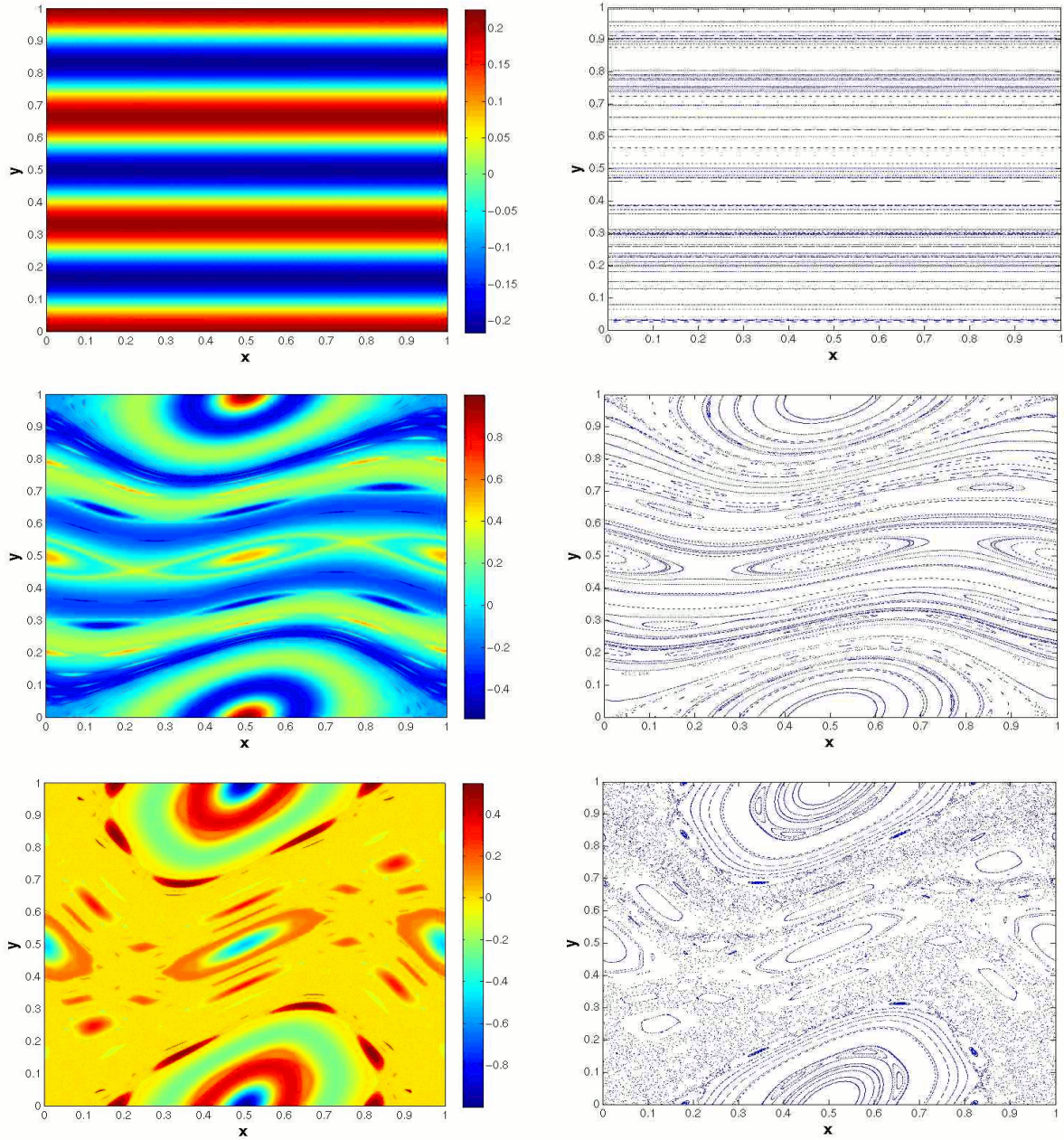


Fig. 1: Color-plots of time averages (left) and the corresponding phase space portraits (right) done as 100 iterations of 11×11 random trajectories picked uniformly from $[0, 1]^2$. Top: $\varepsilon = 0$ for the function $\sin(3\pi x + 6\pi y)$, middle: $\varepsilon = 0.09$ and $\sin(5\pi x + 8\pi y)$, bottom: $\varepsilon = 0.18$ and $\sin(3\pi x + 8\pi y)$.

rotation - on them). Accordingly, the plot is a family of horizontal single-color lines, with color depending on the time average of the function over each $y = \text{const.}$ line. Middle figures show the case of $\varepsilon = 0.09$ where the phase space is a mix between a small chaotic zone and families of regular islands. Note how coloring diversity of time averages gives more insight into the phase space structure than the usual phase portrait - the color-plot predicts correctly full dynamical structure of the phase space. The bottom two figures regard the case of $\varepsilon = 0.18$ characterized by the presence of a large chaotic zone, which is uniformly colored (as expected).

Some independent invariant sets appear colored with the same color in some plots. Since the averaged functions are oscillatory, they can yield the same time averages in dynamically different regions. This is why a single time average plot does not uniquely identify an ergodic set: this problem will be addressed later by employing more functions.

3.2 The Wavelet orthogonal basis

As a further illustration of our method, we employ functions from the *Haar wavelet* basis in 2D. Wavelets are a multi-scale functional family used in frequency decomposition and multi-resolution analysis [25]. In 1D, the Haar wavelet basis is constructed from the *mother wavelet* ψ_{00} , defined by:

$$\psi_{00}(x) = \begin{cases} -1 & \text{if } x \in [0, \frac{1}{2}] \\ 1 & \text{if } x \in]\frac{1}{2}, 1[\\ 0 & \text{if } x \in \mathbb{R} \setminus [0, 1] \end{cases}$$

A general 1D wavelet ψ_{ij} is constructed from this one by the appropriate transformations, summarized as:

$$\psi_{ij}(x) := 2^{i/2} \psi_{00}(2^i x - 2^{-i} j),$$

and, as it can be shown, the functional family $\{\psi_{ij}\}_{i,j \in \mathbb{Z}}$ is a basis for $L^2(\mathbb{R})$. The 2D wavelets are constructed as cross-products of 1D wavelets (in case 2D functional family is to be a basis for $L^2(\mathbb{R}^2)$, the procedure also involves cross-products of 1D wavelets with 1D *scaling functions*; we shall however skip these technical details, and refer the reader to [25] and references therein). For the purposes of our study, we construct and use the 2D wavelet function called W :

$$W = 2^{\frac{1}{3}} \sum_{n,m=1}^8 \psi_{3n} \otimes \psi_{3m} = \sum_{n,m=1}^8 \psi_{00}(8x - \frac{n}{8}) \otimes \psi_{00}(8x - \frac{m}{8}),$$

whose graph is shown in Fig. 2a. Clearly, W can be constructed from the 2D wavelets basis.

In Figs. 2b,c&d we show time averages of W under the standard map dynamics Eq.(7) for various values of ε , using the same grid and total iterations. It is again easy to recognize the known standard map features visible through diverse coloration of the phase space regions. As opposed to the Fourier functions case, wavelet functions have "sharp edges", which is why these plots have more drastic coloration changes among closely located invariant sets (compare Fig. 2b to the middle plot in Fig. 1 regarding $\varepsilon = 0.09$, and Fig. 2d to the

last plot in Fig. 1 regarding $\varepsilon = 0.18$). This property can be used for "zooming" (see Section 5.), i.e. in the case when a specific phase space sub-region is to be examined. It is interesting to note that the chaotic region for $\varepsilon = 0.16$ (cf. Fig. 2c) is not uniformly colored despite that ε is above the chaotic transition value - as the transport throughout the chaotic region is still slow in the area around the last broken KAM curve, a different coloration occurs there. This non-uniform structuring of the chaotic zone is known as Markov tree model in Hamiltonian maps [26].

In order to investigate the phase space structure at larger (smaller) scale, one preferably takes smaller (bigger) Fourier/wavelet frequency (that is 3 in this case). In the context of standard map it is convenient to use a slightly bigger frequency for y coordinate - since the transport in x direction is much faster, the function averages out to zero rather quickly in this direction. While the Fourier functions give smoothly colored plots, wavelets produce sharper and more detailed plots with a better distinction between the independent invariant sets. However, different invariant sets still happen to be assigned the same colors, rendering impossible to simultaneously visualize local and global phase space structures.

4 The Convergence Properties

In this Section we study the convergence properties of the time averages in order to estimate the precision of the values obtained and relate them to the different types of orbits. For simplicity we use only Fourier functions (the results for wavelets are similar). Consider the n -th partial time average for a function f given by:

$$f^n(x_0, y_0) = \frac{1}{n} \sum_{k=0}^{n-1} f(\mathbf{T}^k(x_0, y_0)), \quad (9)$$

with $\lim_{n \rightarrow \infty} f^n(x_0, y_0) = f^*(x_0, y_0)$ (which we assume exists for all grid-points (x_0, y_0)). The difference:

$$\Delta_n(\mathbf{x}) = |f^*(x_0, y_0) - f^n(x_0, y_0)| \quad (10)$$

is a sequence whose asymptotic behavior is to be studied in relation to the initial point (x_0, y_0) and the ε -value, deferring between the phase space regions having different dynamical behaviors. We define $f^* = f^{n=10^7}$ and consider the first 10^6 iterations.

The Regular Region. For all the points on the regular trajectories the time averages converge with the error decreasing as $\frac{a}{n}$, with the constant a given by the trajectory properties, as shown in [19]. The result applies uniformly to all the regular orbits in the case of dynamics Eq. (7) regardless of the ε -value and the choice of function. Given that $a \sim O(1)$ this allows a rather precise estimation of the final precision of the obtained time average value, in relation to the total number of iterations computed n_{final} . A typical convergence plot for the case of a regular trajectory is reported in Fig. 3a.

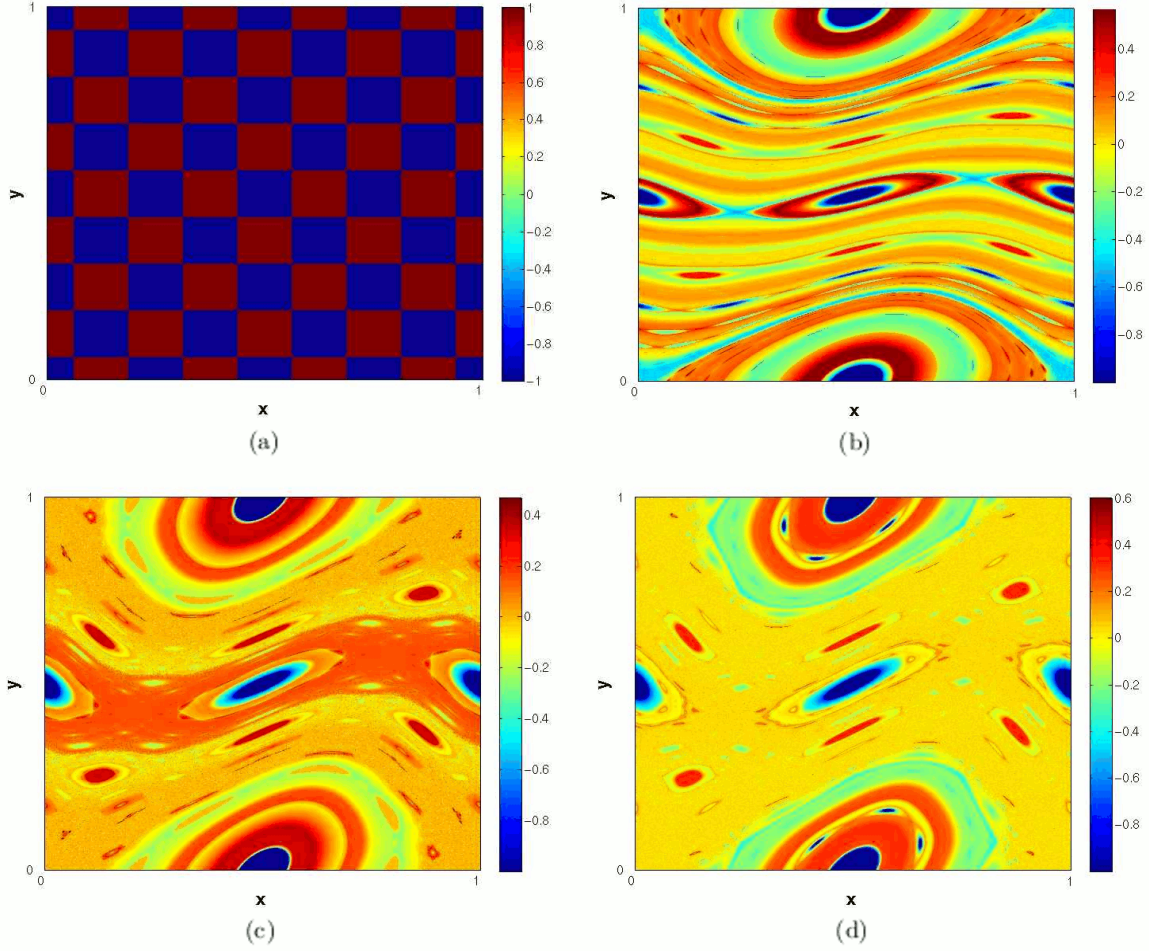


Fig. 2: The graph of the wavelet W in (a). Its time average for $\varepsilon = 0.09$ in (b), $\varepsilon = 0.16$ in (c) and $\varepsilon = 0.18$ in (d).

Strongly Chaotic Region. In the case of strong mixing the fluctuations of the time average decrease as $\frac{1}{\sqrt{n}}$ [19]. In the context of the dynamics Eq. (7) this implies the expected convergence rate to be at best given by this estimate. Our findings indicate this rate asymptotically approaches n^α regime with $\alpha \gtrsim -\frac{1}{2}$; the $\alpha = -\frac{1}{2}$ result was obtained only in the case of very chaotic orbits (large ε). A typical convergence plot for a chaotic trajectory is shown in Fig. 3b. Given the mixed phase space of map Eq. (7), the plot exhibits a very irregular behavior, which is bounded by the n^α regime away from the transients. Hence, the error in the case of chaotic time averages can be estimated from below by $1/\sqrt{n_{\text{final}}}$ and improved by the increase of the ε -value.

Weakly Chaotic Region. Below the chaotic transition for Eq. (7) ($\varepsilon \lesssim 0.15$), the chaotic regions are localized in the phase space around the hyperbolic fixed points, and characterized by a weak chaos with trajectories slowly diffusing through the region. The convergence of the time averages in this region is extremely slow and irregular, and cannot be in general bounded by any asymptotic slope of n^α type. A

typical convergence plot for this region is reported in Fig. 3c. Note that despite plot showing less irregular oscillations than in the strongly chaotic case, it barely decreases and cannot be fitted with a determined slope. This convergence pattern is consistently present in all the weak chaos trajectories, and it improves only with the increase of ε -values. It is therefore hard to estimate the final error in this case, unless the dynamics is run for excessively long times. Our visualization method appears to suit better the cases of either regular or strongly chaotic behavior where the “speed” of filling the invariant set is relatively high. Yet, given that the phase space size of weakly chaotic regions is typically small, one can still have a good overall precision of the plots for small ε -values.

In conclusion, the precision obtained for weakly chaotic trajectories will determine the least bound for the precision of the time average plots as the ones in Figs. 1 and 2. However, given a very limited number of grid-points in this region of the phase space, one can set the total number of iterations according to the precision rates of the strongly chaotic zone. In this spirit we take $n_{\text{final}} = 30,000$ iterations: this sets

the precision of strongly chaotic case to $O(10^{-2})$ (with even better precision for the regular case), which is enough given that the considered functions have values in the $[-1, 1]$ interval. Note also that the convergence properties show a certain

pattern in relation to the trajectory type: it would be possible to characterize the nature of a trajectory by looking at this patterns for different functions (which is closely related to the work of Melbourne and Gottwald [27]).

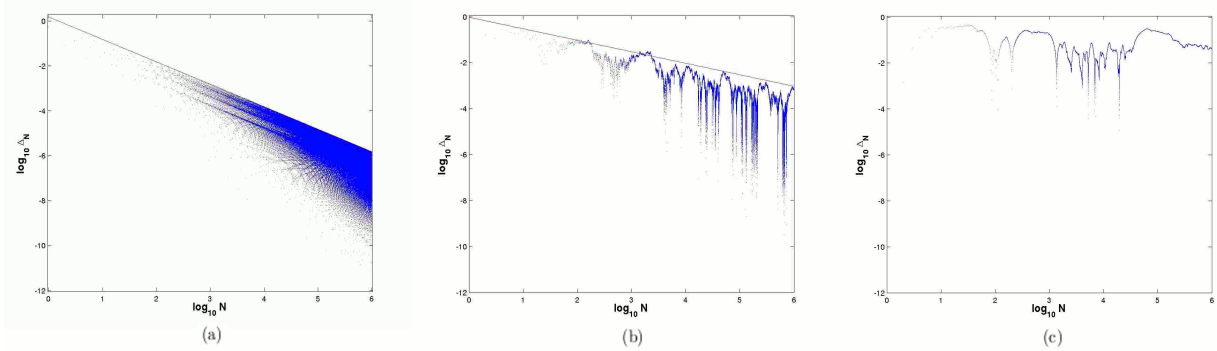


Fig. 3: The convergence plots for a regular orbit with $\varepsilon = 0.12$ and $f(x, y) = \sin(2\pi x + 2\pi y)$ for the initial point $(0.59, 0.38)$ fitted with the slope of -1 in (a), a strongly chaotic orbit with $\varepsilon = 0.54$ and $f(x, y) = \sin(\pi x + 3\pi y)$ for $(0.11, 0.08)$ fitted with the slope of $-\frac{1}{2}$ in (b) and a weakly chaotic orbit with $\varepsilon = 0.12$ and $f(x, y) = \sin(2\pi x + 4\pi y)$ for $(0.001, 0.003)$ in (c).

5 The Clustering Methods and Visualization

In this Section the time averages of N (linearly independent) functions are considered for the dynamics Eq. (7), and the correspondence given by Eq. (6) is studied. We investigate the distribution and clustering of time average vectors $\mathbf{f}(x_0, y_0) \in [-1, 1]^N$ by constructing scatter plots with two or more functions. We furthermore design a simple algorithm for approximation of the phase space ergodic partitioning.

5.1 Scatter plots with $N = 2$

We consider Fourier functions and begin by the simple case of $N = 2$. Time averages f_1^* and f_2^* are computed for every grid-point defining the correspondence between the grid-points (x_0, y_0) and the time average vector $\{f_1^*, f_2^*\}$:

$$(x_0, y_0) \in \text{grid} \longrightarrow \{f_1^*, f_2^*\} \in [-1, 1]^2.$$

The *scatter plot* is obtained by plotting all the vectors $\{f_1^*, f_2^*\}$ on the square $[-1, 1]^2$. We use the same grid and total iterations as before. The idea is illustrated in Fig. 4 where a scatter plot involving two functions is investigated with reference to the corresponding time averages plots and the phase space portrait. As already stated, each single point in the scatter plot has the x -coordinate equal to $f_1^*(x_0, y_0)$ and the y -coordinate equal to $f_2^*(x_0, y_0)$ for some grid-point (x_0, y_0) . As indicated in the figure, long branches (curves)

represent the families of periodic islands around elliptic fixed points, while the irregular clouds amount for localized chaos around the hyperbolic fixed points. Secondary chaotic zones appearing around second-order hyperbolic points are also visible, together with the secondary families of periodic orbits.

To investigate this further we show the same scatter plot for the same time averages, zoomed to the phase space region $[0.6, 0.9] \times [0.6, 0.9]$ in Fig. 5. The scatter plot can readily be recognized as a part of the scatter plot from Fig. 4. Again, we see the interplay between long curved lines and irregular clouds, representing regular and chaotic regions respectively. Note that many more secondary periodic families are visible in this plot due to the improved resolution (zoom), capturing the scale-invariant fractal nature of the standard map's phase space.

The scatter plots in Figs. 4 and 5 are transforming the dynamical complexity of the standard map into the geometrical complexity of the scatter plots. A two-function scatter plot is an embedding of time average vectors into \mathbb{R}^2 which provides a second-order approximation of ergodic sets (as opposed to the first-order approximation given by a single-function plot). While the addition of a function improves the quality of embedding, the increase of number of iterations increases the precision of a scatter plot - the time average vectors contained in each small neighborhood on it correspond to a set of grid-points which together form a second-order approximation of an invariant set.

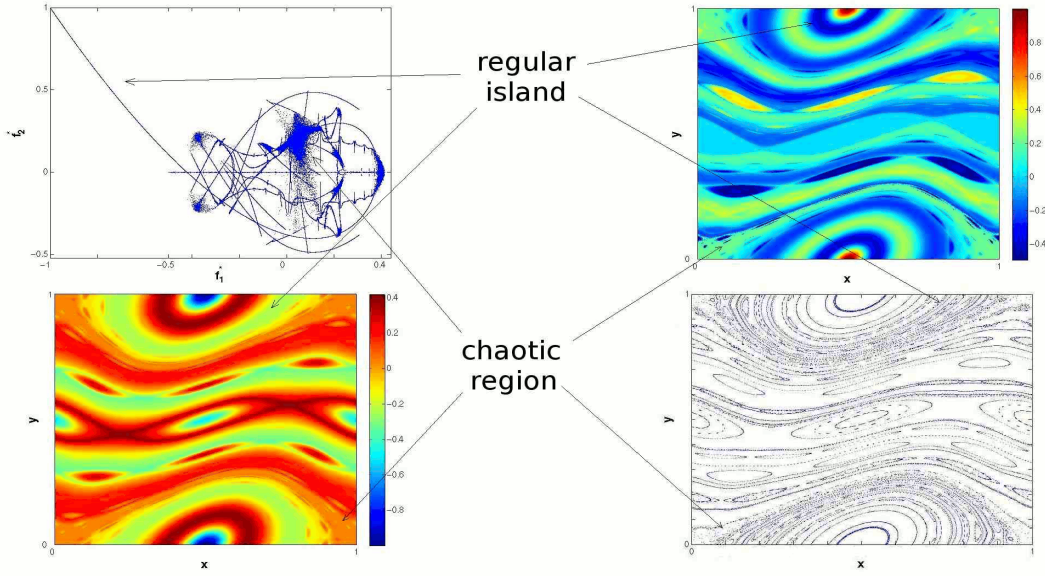


Fig. 4: Two-function scatter plot for $\varepsilon = 0.12$, with $f_1 = \sin(3\pi x + 8\pi y)$ and $f_2 = \sin(7\pi x + 9\pi y)$. Phase space dynamical regions are indicated along with the corresponding scatter plot parts.

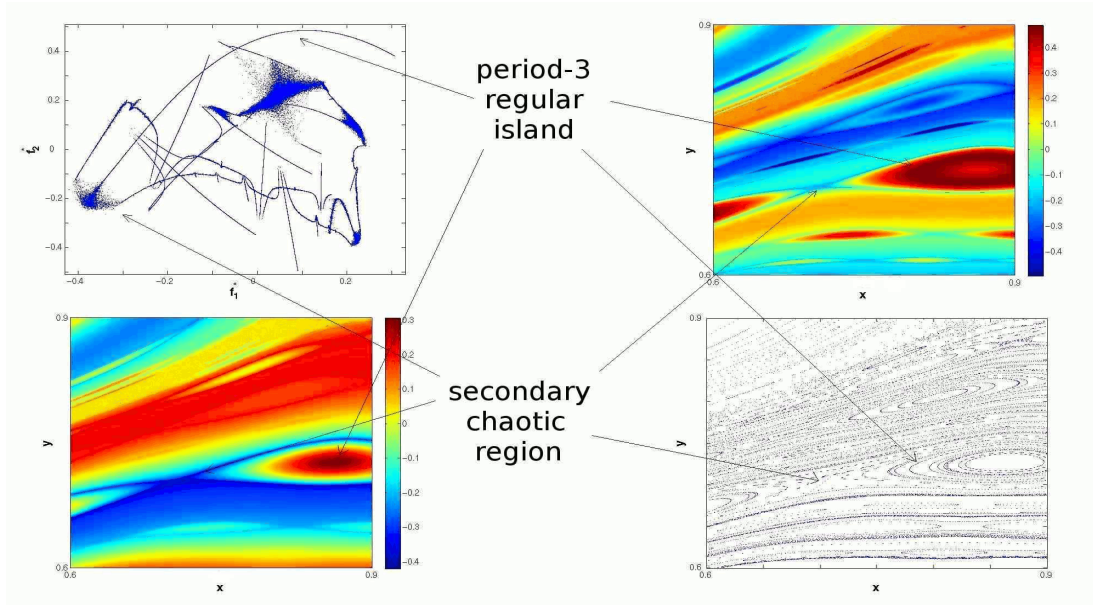


Fig. 5: A zoom of the scatter plot from Fig. 4 for the phase space region $[0.6, 0.9] \times [0.6, 0.9]$. Dynamical regions and their corresponding scatter plot parts are indicated.

5.2 Scatter plots in 3D

We set $N = 3$ and consider the scatter plots done with three linearly independent functions. We use 300×300 initial grid and the same total iterations as previously, considering the correspondence:

$$(x_0, y_0) \in \text{grid} \longrightarrow \{f_1^*, f_2^*, f_3^*\} \in [-1, 1]^3.$$

In Fig. 6 we show nine scatter plots obtained for the three functions and increasing ε -values. We monitor the phase space structure evolution as ε is changed, in terms of geometric complexity evolution of the scatter plot's structure. Note the changes in branches and development of higher order periodic islands, with localized chaotic zones around hyperbolic fixed points at joints between different families of periodic orbits.

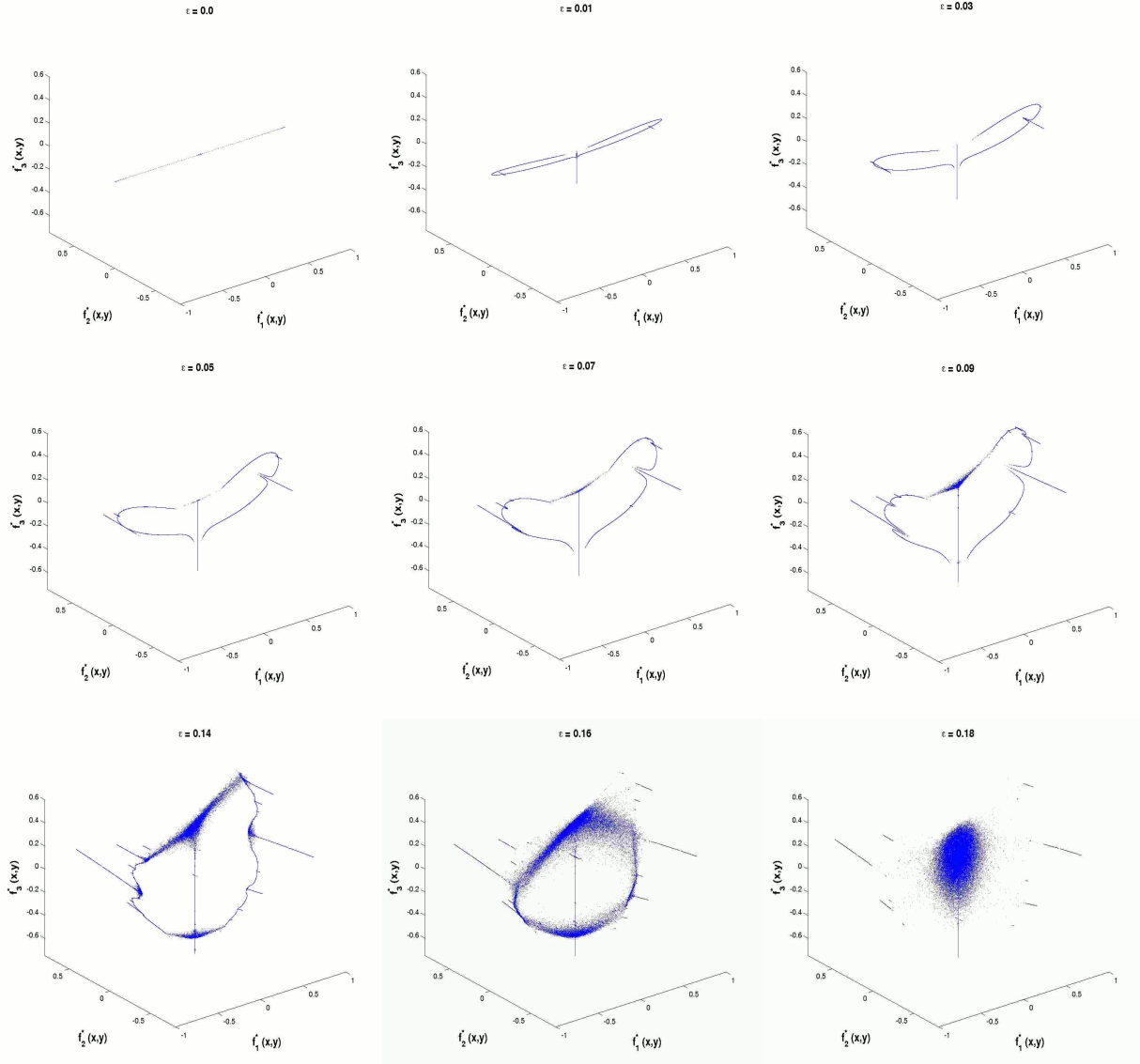


Fig. 6: 3D scatter plots for $\sin(2\pi y)$ vs. $\sin(4\pi x + 4\pi y)$ vs. $\sin(2\pi x + 3\pi y)$ with ε indicated in each plot.

The chaotic transition occurring for $\varepsilon \simeq 0.15$ can here be seen as a merging of localized chaotic zones that propagate along the branches into a single connected chaotic zone. As expected, at the strongly chaotic regime all the time average vectors are localized in a single cluster that shrinks in size with further increase of ε . In the case of ergodic behavior one expects all the time average vectors to overlap in a single point in $[-1, 1]^3$ space. Adding a function to the scatter plot clearly improves the representation of the phase space structure, by increasing the embedding dimension. Furthermore, the Fig. 6 shows the sufficient embedding dimension for the standard map's scatter plots to be three: it is in three

dimensions where the families of regular orbits can be fully represented without intersecting themselves.

Finally, in Fig. 7 we examine the time-evolution of the large time average vectors cluster corresponding to the chaotic region at $\varepsilon = 0.18$, as the one in last plot on Fig. 6. We locate the center of the cluster and observe the distribution of distances of the time average vectors from it, in function of the number of iterations. Fig. 7a shows the evolution of that distribution, while in Fig. 7b we consider the evolution of the distribution's peaks with time. Clearly, we recover the $1/\sqrt{n}$ law as expected for the chaotic region, reconfirming the convergence rates conclusions from the Section 4.

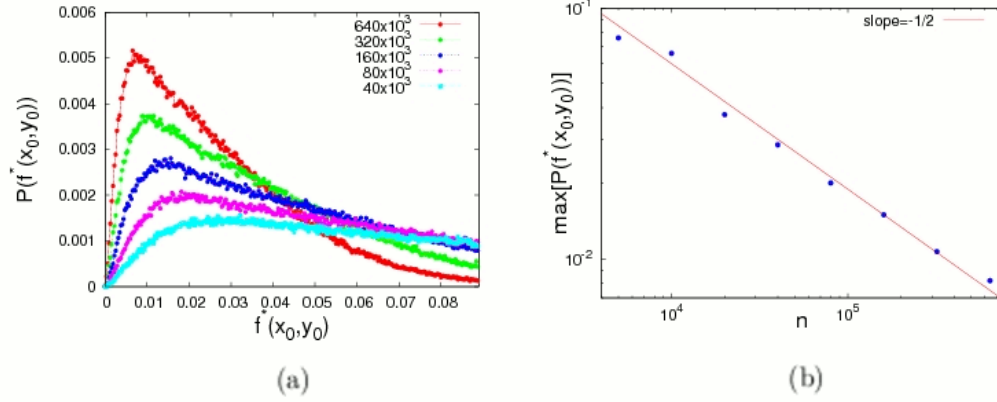


Fig. 7: (a): Time-evolution of the distribution of distances from the cluster-center for the time average vector cluster corresponding to the chaotic zone for $\varepsilon = 0.18$ (cf. last plot on Fig. 6). Functions used are $f_1 = \sin(\pi x + 2\pi y)$, $f_2 = \sin(3\pi x + 2\pi y)$ and $f_3 = \sin(3\pi x + 8\pi y)$ for the iteration times as indicated. (b): time-evolution of the distribution peaks from (a), fitted with $-\frac{1}{2}$ slope.

5.3 Visualization of the ergodic partition via clustering

Following the investigation of the scatter plots we construct a simple algorithm for approximation of the ergodic partition and its graphical phase space visualization. Consider an N -function scatter plot contained in $[-1, 1]^N$:

- step 1 divide the N -cube $[-1, 1]^N$ into L^N cells dividing each axis into L segments as illustrated in Fig. 8a (for $N = 2$ and $L = 16$), and consider the distribution of time average vectors around the cells
- step 2 disregard the cells that contain no time average vectors
- step 3 assign a color to every remaining cell, therefore assigning a color to every time average vector
- step 4 observe the grid-points corresponding to time average vectors sharing a cell/color: they define an N -order approximation of an ergodic set
- step 5 color the phase space by coloring each grid-point with the color assigned to it

Note that this is a generalization of the single-function coloring scheme with a difference that now the scheme is regulated by adjusting the cell division and optimizing it according to the structure of the scatter plot. The smoothness of the coloring is lost (as nearby invariant sets might have their time average vectors in different cells), but the multi-dimensionality of the color-assigning rule is gained, allowing for differentiation among the invariant sets.

We examine the scatter plot from the Fig. 4 (with the same grid and total iterations), showing it in Fig. 8a with 16×16 cells division. The corresponding approximation of

the ergodic partition with colors between blue and red randomly assigned to non-empty cells is shown in Fig. 8b. A better overall clarity of the invariant set structure is obtained both at the global and local level (within the approximation precision, which is also influenced by a limited number of available colors). Note that the visibility can be enhanced by coloring nearby invariant sets with different colors which is attained by randomizing the color-assignment for the non-empty cells. The number of visualized set increases with increase of L (Figs. 8b&c), but the color differentiation gets poorer, as the number of available (visible) colors remains limited (not only by the software, but also by the human eye recognition). The optimal value of L (regulating the number of cells) is to be set according to the visualization requirements, taking into account the relationship between color differentiation vs. number of visible invariant sets. For the two-function case examined in Fig. 8, it appears the optimal L is around 35 (corresponding to Fig. 8c). Too small L is underusing the scatter plot as it colors too many different invariant sets uniformly (Fig. 8b), while for too large values of L the lack of colors brings the same problem, in addition to a too non-uniform coloration of the chaotic region (Fig. 8d).

In Fig. 9a we show an example of ergodic partition approximation constructed from a three-function scatter plot, using the functions from Fig. 8 case as the first two. Note that for $L = 30$ we obtain a better quality than previously. Finally, in Fig. 9b we add another function and show a four-function approximation obtained for the optimal L value of $L = 35$.

As noted earlier, we have chosen functions involving different frequencies, thus visualizing global and local phase space features simultaneously. Figs. 9a&b reveal high-resolution approximations to the ergodic partitions for $\varepsilon = 0.12$, producing good approximations to the invariant set structure of the standard map's phase space.

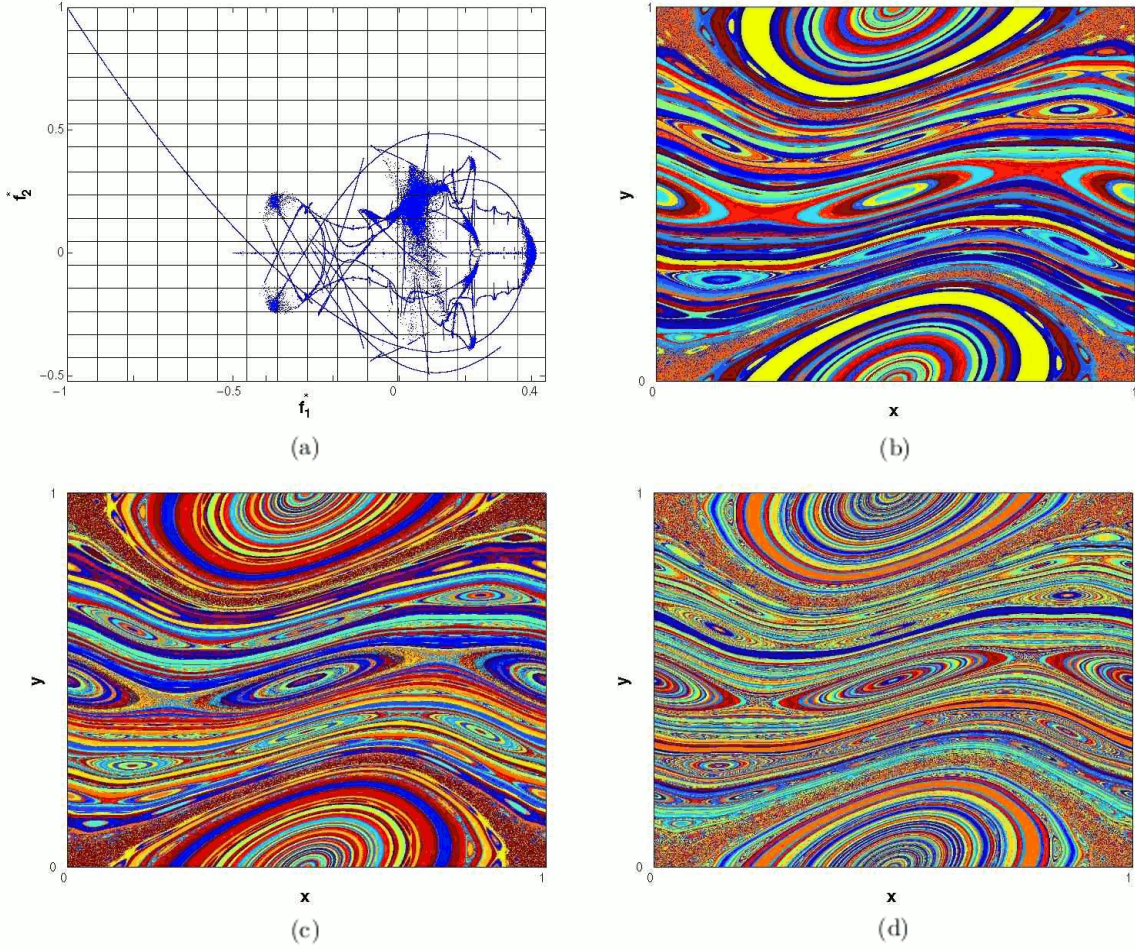


Fig. 8: Scatter plot from Fig. 4 divided into 16×16 cells in (a) and the ergodic partition corresponding to it in (b). The same scatter plot with 34×34 and 83×83 cell divisions in (c) and (d), respectively. Colors were assigned to the non-empty cells randomly from the uniform distribution $[0, 1]$ (0-blue, 1-red).

Note that both pictures indeed visualize details at all scales, with the Fig. 9b being somewhat sharper. In construction of these plots we sought to improve the cell division by having a relatively uniform number of time average vectors within each cell, in relation to the available colors. Due to a particular choice of functions, in Fig. 9b we managed to obtain good coloration for $L = 35$ (very large value considering the number of functions involved), creating the optimal approximation for the four-function case. Given the number of invariant sets visualized, different realizations of random colors assignments make very little difference in the overall picture.

The software's limited number of available colors still makes some different ergodic sets appear in the same color; this problem can be partially overcome by optimizing the color-assigning rule. Instead of assigning a random color to each non-empty cell one could create an assigning-algorithm that would be optimized in relation to the particular case studied. Another problem arises in relation to the ergodic

zone in the phase space: given that its time average vectors are more diffused than the regular orbits' ones (cf. Fig. 6), they set the lower bound to the size of the cells. This is why the ergodic zone in the Fig. 8d appears non-uniformly colored. In the context of the standard map, it is convenient to pick a smaller L for low ε -values in order to obtain a better focus on the nested invariant curves, while for larger ε -values a bigger L allows to include the whole chaotic zone in a single cell/color. Also, a bigger number of functions allows more flexibility for the L -value as the underlying scatter plot differentiates better among the invariant sets. Moreover, a better cell division scheme would not employ the simple cubical division described here, but a more sophisticated algorithm optimizing (for instance) the number of time average vectors per cell with respect to their distance in the time average space. One could also seek to adjust the shape of cell according to the properties of the scatter plot instead of just using the simple cubical ones.

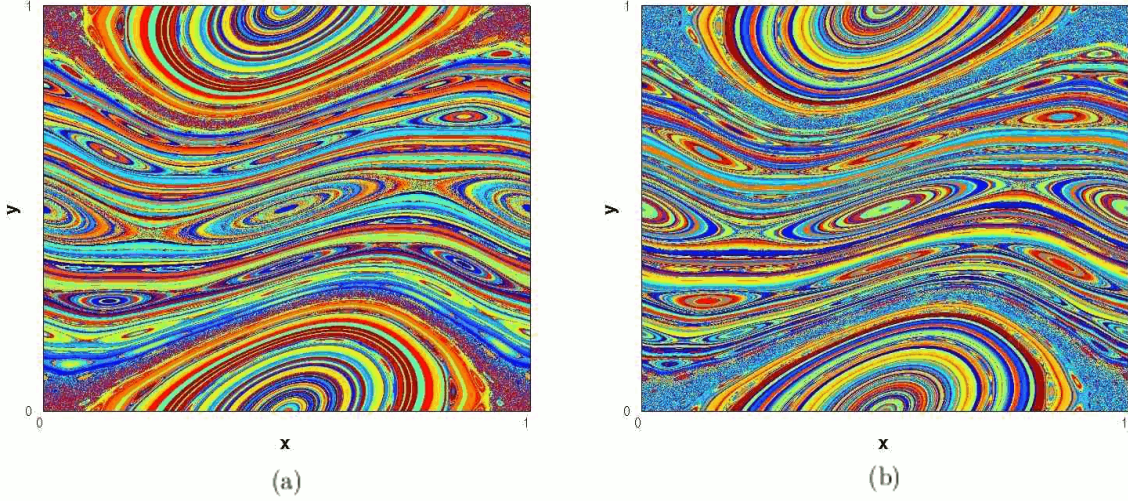


Fig. 9: Three-function ergodic partition approximation using $f_1 = \sin(3\pi x + 8\pi y)$, $f_2 = \sin(7\pi x + 9\pi y)$ and $f_3 = \sin(3\pi x + 6\pi y)$ with $\varepsilon = 0.12$ and $L = 30$ in (a). Four-function approximation using additional $f_4 = \sin(5\pi x + 4\pi y)$ and $L = 35$ in (b). The colors were assigned randomly as in the previous case.

Furthermore, a problem of limited number of colors could be tackled by employing a specific graphically-oriented visualization software allowing more flexibility in terms of choosing or adjusting colors and their tones. Also, a cell's color could be determined in relation to the number of time average vectors contained in it, or contained in the neighboring cells, thus differentiating better among various invariant sets.

Finally, in the case of measure-preserving maps with a given maximum scatter plot embedding dimension (three in this case, cf. Fig. 6), one could seek to parametrize the scatter plot obtaining a continuous coloration scheme that would include all the invariant sets. Still, this procedure would yield a non-uniform number of time average vectors per cell, allowing for further improvements. For the purpose of this study however, we limit ourselves to the simple and illustrative algorithm just exposed.

6 The Froeschlé Map

As our first higher-dimensional example we consider 4D measure-preserving Froeschlé map [21] that consists of two standard maps with a symplectic coupling:

$$\begin{aligned} x'_1 &= x_1 + y_1 + \varepsilon_1 \sin(2\pi x_1) + \eta \sin(2\pi x_1 + 2\pi x_2) \\ y'_1 &= y_1 + \varepsilon_1 \sin(2\pi x_1) + \eta \sin(2\pi x_1 + 2\pi x_2) \\ x'_2 &= x_2 + y_2 + \varepsilon_2 \sin(2\pi x_2) + \eta \sin(2\pi x_1 + 2\pi x_2) \\ y'_2 &= y_2 + \varepsilon_2 \sin(2\pi x_2) + \eta \sin(2\pi x_1 + 2\pi x_2) \end{aligned} \quad (11)$$

where $(x_1, y_1, x_2, y_2) \in [0, 1]^4$. We set $\varepsilon_1 = \varepsilon_2 = \varepsilon$ and reduce our investigation to the case of two identical interacting standard maps. Given its structure, a convenient way to study the map Eq. (11) is by comparison with the standard map's phase space in terms of the coupling parameter η . To that end we fix a phase space 2D section in map's (x_2, y_2) -space, and consider the time averages of functions using a

two-dimensional grid having constant (x_2, y_2) values. A grid of 500×500 initial grid-points is set in (x_1, y_1) -space and the dynamics is iterated for 100,000 iterations. The results are shown in Fig. 10 where the parameter η is varied for a fixed value of ε . Note the departure from the known standard map's phase space (Fig. 10a) due to increasing interaction between the maps. For small η values, the phase space apparently maintains its regular structure with only small and localized chaos (Figs. 10b&c), similarly to standard map for small ε . The coloring here indicates 2D projections of the 4D invariant sets of the map Eq. (11): we are visualizing the intersections of real 4D invariant sets with the chosen 2D phase space section. Nevertheless, the invariant set section still provides a lot of insight into dynamics' structure.

Furthermore, we examine the three-function scatter plots for the Froeschlé map, by employing 4D grid of $20 \times 20 \times 20 \times 20$ initial grid-points and the same number of total iterations. In Fig. 11 we consider structural changes in the scatter plots with $\eta = 0$ by changing the ε -value. Observe the development of surfaces representing invariant tori of two uncoupled standard maps for small ε -values. In Fig. 12 we show a sequence of scatter plots with a fixed $\varepsilon = 0.01$ and increasing η ($\eta = 0$ case for this ε is shown in Fig. 11). Note the destruction of surfaces from Fig. 11 by increase of inter-map coupling η . The scatter plot's structure reports a given level of regularity in the phase space persisting for a certain range of coupling parameter strengths. This is a manifestation of KAM nature of this map, which (similarly to the standard map) maintains some invariant tori until the parameters exceed certain thresholds. For convenience, we consider functions in the y -coordinates only (action variables), seeking to visualize parts of invariant torus parametrized by two actions y_1 and y_2 (cf. last few scatter plots in Fig. 11).

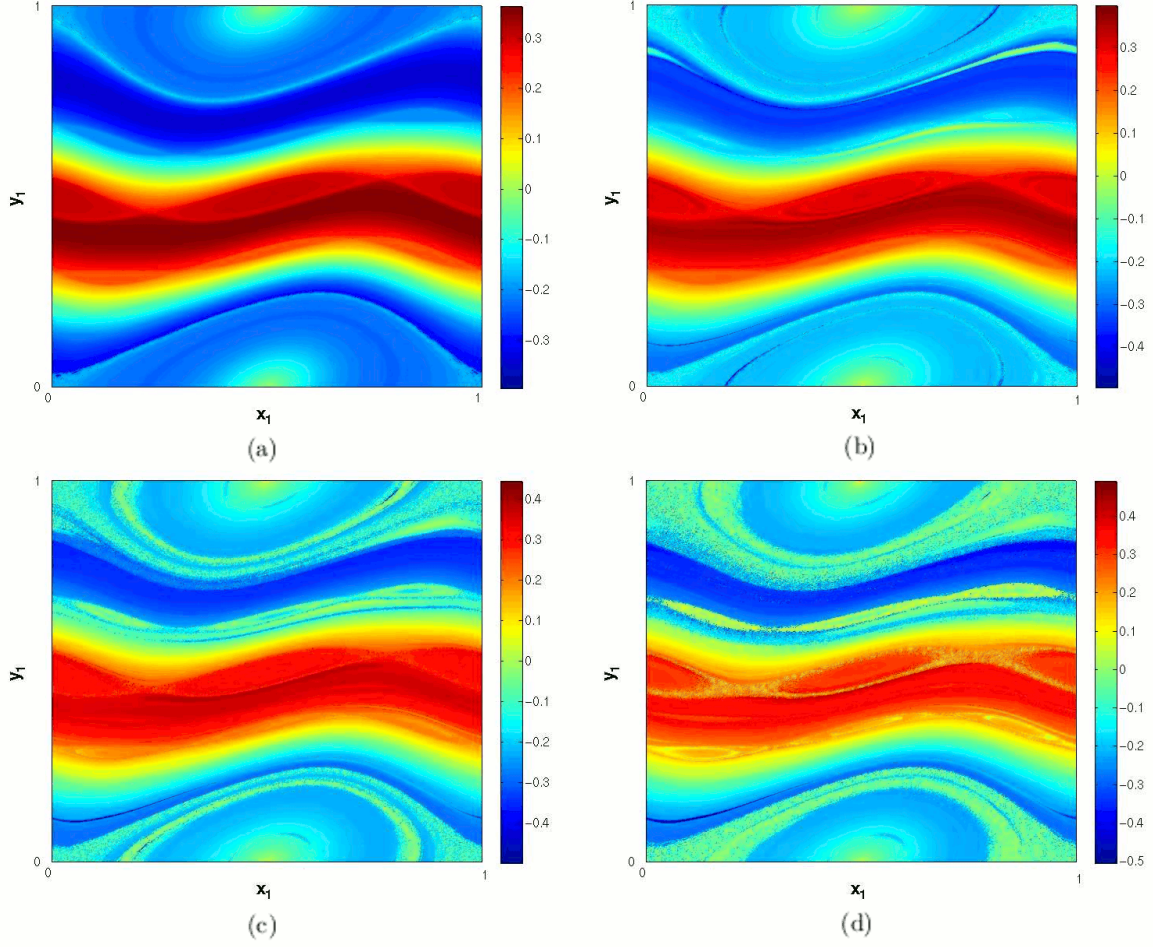


Fig. 10: Time averages of $f(x_1, y_1, x_2, y_2) = \sin(3y_1 + 7y_2)$ for the fixed section $(x_2, y_2) = (0.75, 0.25)$, with $\varepsilon = 0.09$ (cf. Fig. 2b), and $\eta = 0$ in (a), $\eta = 0.0001$ in (b), $\eta = 0.0005$ in (c) and $\eta = 0.001$ in (d).

We conclude the Section by observing that scatter plot analysis as employed here allows investigations of systems much more complex than the standard map. As pointed out previously, with an appropriate choice of functions one can reduce the complexity of a given system to geometrical features of the scatter plot, capturing the key dynamical details of the system in the form of scatter plot structure. Moreover, various changes in system's properties can be monitored this way (cf. Fig. 12) by observing the geometrical evolution of the scatter plot. A further application of this technique might be in the study of complex dynamical systems, like the coupled maps on networks [24].

7 Extended Standard Map

As a second higher-dimensional example we consider the 3D extended standard map [22], that represents a generaliza-

tion of the classical standard map. It is a volume-preserving action-action-angle map defined as:

$$\begin{aligned} x' &= x + \varepsilon \sin(2\pi z) + \delta \sin(2\pi y) & [mod\ 1] \\ y' &= y + \varepsilon \sin(2\pi z) & [mod\ 1] \\ z' &= z + x + \varepsilon \sin(2\pi z) + \delta \sin(2\pi y) & [mod\ 1] \end{aligned} \quad (12)$$

with the values in $[0, 1]^3$. Its physical origin and the analytical properties are investigated in [22]. For $\delta = 0$ the map takes the form:

$$\begin{aligned} x' &= x + \varepsilon \sin(2\pi z) & [mod\ 1] \\ y' &= y + \varepsilon \sin(2\pi z) & [mod\ 1] \\ z' &= z + x + \varepsilon \sin(2\pi z) & [mod\ 1] \end{aligned} \quad (13)$$

which keeps the planes $y - x = const.$ invariant under the dynamics, and reduces to the standard map in x and z coordinates (while y behaves like another action coordinate).

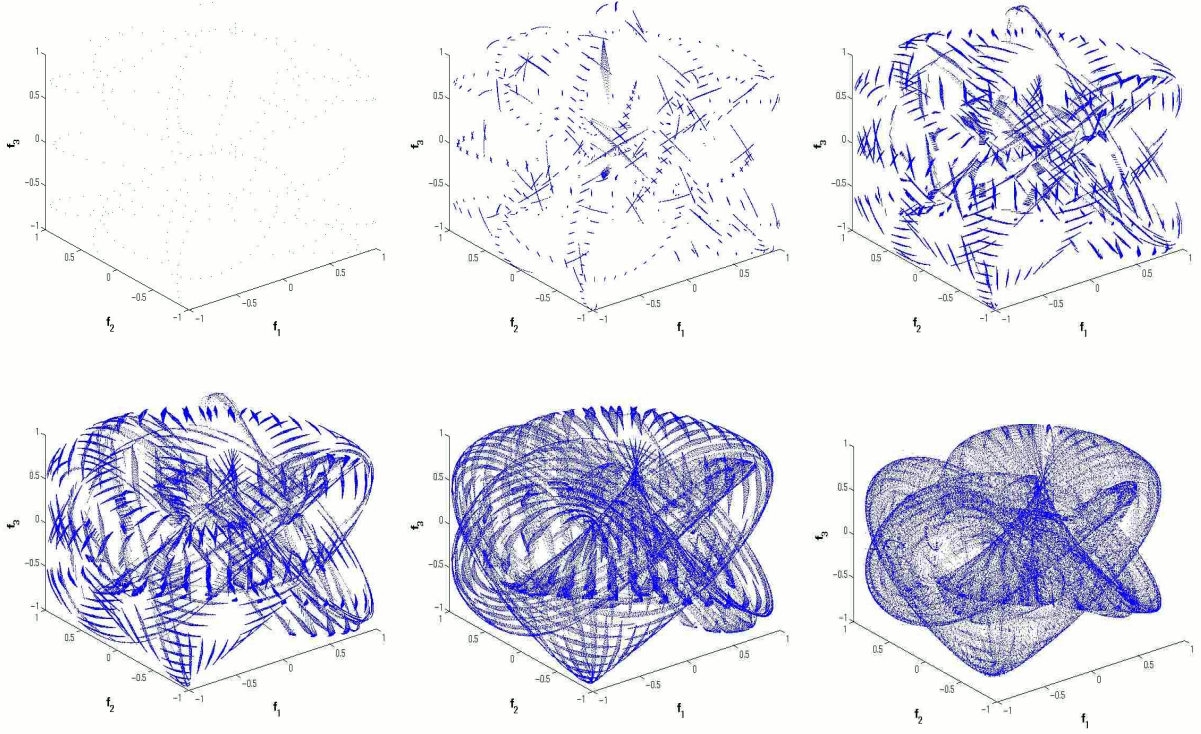


Fig. 11: Sequence of three-function scatter plots for $f_1 = \sin(3y_1 + 2y_2)$, $f_1 = \sin(4y_1 + 5y_2)$ and $f_1 = \sin(5y_1 + 5y_2)$, with $\eta = 0$ fixed and ε respectively 0, 0.001, 0.005, 0.01, 0.02, 0.05.

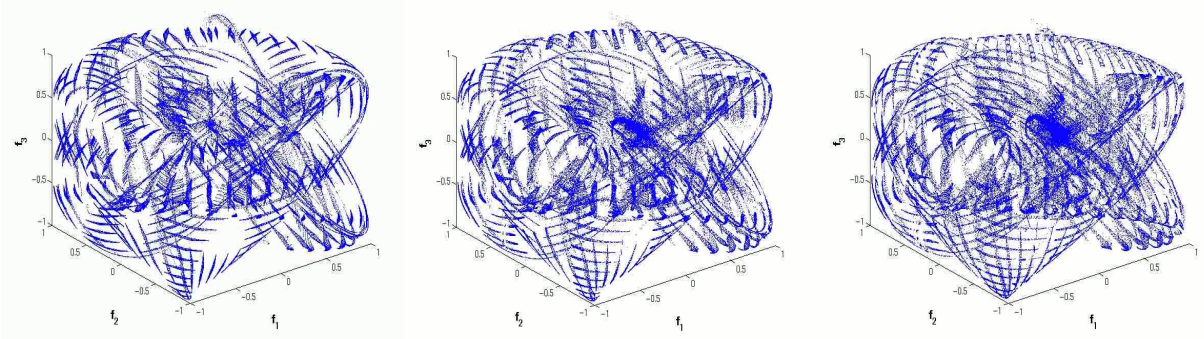


Fig. 12: Sequence of three-function scatter plots using the same functions from Fig. 11, with $\varepsilon = 0.01$ fixed, and η respectively 0.0001, 0.005, 0.01.

This structured family of standard maps on diagonal planes is however broken for $\delta > 0$ as the transport is allowed between the diagonal planes. Actually, as conjectured in [22] the extended standard map Eq. (12) is ergodic for any positive values of perturbations ε and δ , with ergodicity being very weak for smaller values.

We bring additional evidence to this claim: consider a three dimensional grid of $41 \times 41 \times 41$ initial grid-points. We compute the time average of this function for two examples of small perturbation values, and report respective histograms of time average values in the Figs. 13a&b. These plots are done with 10^7 and 1.6×10^7 iterations respectively (taking almost 20 hours with full processor capacity), giving a Gaus-

sian distributions of time average vectors strongly peaked around zero. We performed the same computation with different functions, obtaining the same result (with slightly different standard deviation). This seems to confirm the mentioned ergodic hypothesis from the computational prospective. It also agrees with the result proved in [22] stating that no invariant two-dimensional surface persists in this map for any positive perturbation value, implying that the map allows a global transport throughout the phase space at any non-zero perturbation. This consideration demonstrates our method to be useful in the context of numerical proofs related to ergodic properties dynamical systems as the one discussed above.

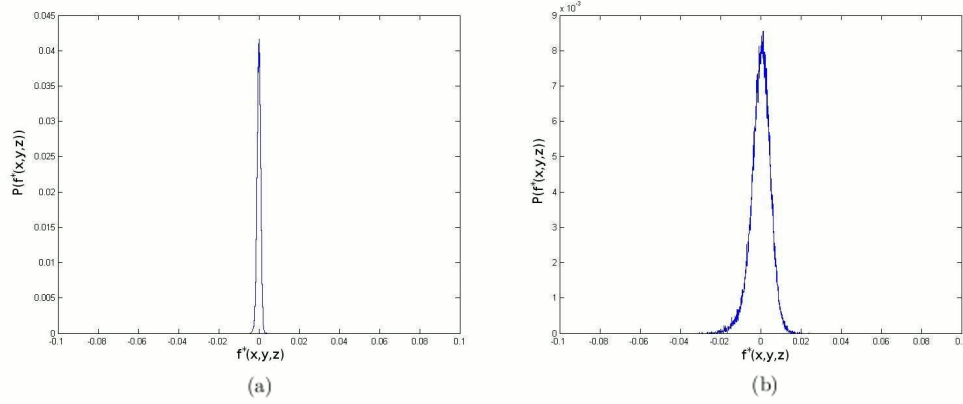


Fig. 13: Histogram of time average values of $f(x, y, z) = \cos(8\pi x + 8\pi y + 8\pi z)$. $\varepsilon = 0.2$ and $\delta = 10^{-4}$ in (a), and $\varepsilon = 0.1$ and $\delta = 10^{-5}$ in (b). In both cases the distribution's mean-value is 0 (up to an error of $O(10^{-4})$) with a standard deviation of $\sigma \sim O(10^{-3})$.

8 Conclusions

We presented the computational realization of an invariant set visualization method based on ergodic partition theory suggested in [1]. The time averages of observables over the dynamics' phase space were computed and visualized using a coloring scheme, for a variety of measure-preserving maps. The time average convergence issues have been considered, providing precision estimations on time average values. Scatter plots of more time averages were shown giving a qualitative view of the global dynamical properties in terms of geometric complexity, for a range of chaotic parameter values. A simple algorithm for approximation of the ergodic partition was developed from multi-functional scatter plots by dividing the time average vectors space in cubical cells. Approximation of ergodic partition and invariant set structure in the phase space was shown for various numbers of functions. By using the standard map with known properties, we were able to confirm the visualization results within the limits of numerical precision. The extent of the method's applicability was illustrated on 4D Froeschlé map and 3D extended standard map, giving new insights into dynamical structure of these systems.

It should be emphasized that the outreach of ergodic theory application for construction of visualization methods in dynamical systems is not exhausted by what is shown in this paper: in the paper to follow [2] we show how periodic sets and resonances can be graphically visualized according to their periodicity and the phase space structure, by the use of *harmonic time averages* that extend the concept of time average described here.

The further improvement of the method primarily lies in the optimization of clustering techniques beyond the simple cell division exposed here: it is of interest to have a flexible coloring scheme that can adopt to different multi-dimensional scatter plot structures, in the sense of optimizing the num-

ber/distance of time average vectors assigned with a given color. The employment of different colorbar schemes is also to be addressed: depending on the system under investigation, the usual red-green-blue coloring used here might not be the optimal one. Also, there is a need for optimal colorbar setting in the sense of coloring organization of cells depending on their location/size in the time average vectors space, as the mere linear colorbar might not suffice. The relationship between the convergence and clustering of time averages is also of importance, as both procedures improve visualization. Moreover, a more detailed geometric analysis of scatter plots structures might yield addition insights into the dynamics, and indicate a way to construct better algorithms for clustering of time average vectors and ergodic partition approximation. This will rely on optimal choice of functions, in relation to the general system's properties and the dynamical coupling parameters in question.

The method can also be applied to the Hamiltonian continuous-time systems for which the ergodic theory results are equally valid, and hence the results shown here apply directly. Of course, the computation of time averages for a continuous-time system is far more numerically demanding. As we have shown, high-dimensional dynamical systems can be studied this way far more easily than with other similar methods through appropriate slicing of the phase space. Another interesting extension includes the issue of time average convergence, namely the relation between various convergence properties and the properties of the underlying dynamics, both for discrete and continuous-time systems. We also suggest that the method is applicable to complex systems like coupled dynamical systems on lattices or networks [24]. Finally, application to recently discovered maps that mimic quantum chaos might be very interesting [29].

Acknowledgments. This work was supported the DFG through the project FOR868, by the AFOSR grant number

F49620-03-1-0096, and by the Program P1-0044 of Ministry of Higher Education, Science and Technology of Republic of Slovenia. Part of this work was done at Department of Theoretical Physics, Jožef Stefan Institute, Ljubljana, Slovenia. Thanks to prof. Bosiljka Tadić and prof. Arkady Pikovsky for useful comments. Thanks to Umesh Vaidya and Giampaolo Cristadoro for constructive discussions.

References

- [1] I. Mezić and S. Wiggins, *Chaos* **9**, 1 (1999).
- [2] Z. Levnajić and I. Mezić, *Arxiv.org*:0808.2182 (2008).
- [3] I. Mezić and A. Banaszuk, *Physica D* **197**, 101 (2004).
- [4] S. Wiggins, *Introduction to Applied Dynamical Systems and Chaos*, Springer-Verlag (1990).
- [5] R.W. Easton, J.D. Meiss and S. Carver, *Chaos* **3**, 2 (1993).
- [6] J. D. Meiss, *Chaos* **7**, 1 (1997).
- [7] M. Dellnitz, A. Hohmann, O. Junge and M. Rumpf, *Chaos* **7**, 2 (1997).
- [8] M. Dellnitz, G. Froyland and O. Junge, in *Ergodic Theory, Analysis, and Efficient Simulation of Dynamical Systems*, Springer (2001).
- [9] B. Thiere and M. Dellnitz, *Ann. N. Y. Acad. Sci.*, 1065 (2005).
- [10] B. Krauskopf and H. M. Osinga, *SIAM J. Appl. Dyn. Syst.* **2**, 4 (2003).
- [11] M. E. Henderson, *SIAM J. Appl. Dyn. Syst.* **4**, 4 (2005).
- [12] B. Krauskopf *et al.*, *Int. J. Bif. Chaos* **15**, 3 (2005).
- [13] P. Walters, *Introduction to Ergodic Theory*, Springer (2000).
- [14] J. P. Eckmann and D. Ruelle, *Rev. Mod. Phys.* **57**, 3 (1985).
- [15] D. D'Alessandro, M. Dahleh and I. Mezić, *IEEE. Trans. Aut. Cont.* **44**, 10 (1999).
- [16] L. Gray and D. Griffeath, *J. Stat. Phys.* **105**, 3-4 (2001).
- [17] M. H. Lee, *Phys. Rev. Lett.* **87**, 250601 (2001).
- [18] O. Jenkinson, *Dis. Cont. Dyn. Sys.* **15**, 1 (2006).
- [19] I. Mezić and F. Sotiropoulos, *Phys. Fluids* **14**, 7 (2002).
- [20] B.V. Chirikov, *Phys. Rep.* **52**, 256 (1979).
- [21] C. Froeschle, *Astron. Astrophys.* **16**, 172 (1972).
- [22] I. Mezić, *Physica D* **154**, 51 (2001).
- [23] J.M. Greene, *J. Math. Phys.* **20**, 1183 (1979).
- [24] Z. Levnajić and B. Tadić, *J. Stat. Mech.*, P03003 (2008).
- [25] G. Kaiser, *A Friendly Guide to Wavelets*, Birkhauser (1994).
- [26] G. Cristadoro and R. Ketzmerick, *Phys. Rev. Lett.* **100**, 184101 (2008).
- [27] G. A. Gottwald and I. Melbourne, *Proc. R. Soc. Lond. A* **460**, 2042 (2004).
- [28] R. Venegeroles, *Phys. Rev. Lett.* **101**, 054102 (2008).
- [29] M. Horvat *et al.*, *Physical D* **238**, 4 (2009).